Characterisation of new gated optical image intensifiers for fluorescence lifetime imaging

H. Sparks, F. Görlitz, D. J. Kelly, S. C. Warren, P. A. Kellett, E. Garcia, A. K. L. Dymoke-Bradshaw, J. D. Hares, M. A. A. Neil, C. Dunsby, and P. M. W. French

Citation: Review of Scientific Instruments **88**, 013707 (2017); doi: 10.1063/1.4973917
View online: http://dx.doi.org/10.1063/1.4973917
View Table of Contents: http://aip.scitation.org/toc/rsi/88/1
Published by the American Institute of Physics

Characterisation of new gated optical image intensifiers for fluorescence lifetime imaging

H. Sparks,[1,a)] F. Görlitz,[1,a)] D. J. Kelly,[1] S. C. Warren,[1] P. A. Kellett,[2] E. Garcia,[1]
A. K. L. Dymoke-Bradshaw,[2] J. D. Hares,[2] M. A. A. Neil,[1] C. Dunsby,[1] and P. M. W. French[1]
[1]*Photonics Group, Department of Physics, Imperial College London, Prince Consort Road, London SW7 2BW, United Kingdom*
[2]*Kentech Instruments Ltd., Howbery Park, Wallingford OX10 8BD, United Kingdom*

(Received 13 June 2016; accepted 26 December 2016; published online 26 January 2017)

We report the characterisation of gated optical image intensifiers for fluorescence lifetime imaging, evaluating the performance of several different prototypes that culminate in a new design that provides improved spatial resolution conferred by the addition of a magnetic field to reduce the lateral spread of photoelectrons on their path between the photocathode and microchannel plate, and higher signal to noise ratio conferred by longer time gates. We also present a methodology to compare these systems and their capabilities, including the quantitative readouts of Förster resonant energy transfer. [http://dx.doi.org/10.1063/1.4973917]

I. INTRODUCTION

Fluorescence lifetime imaging (FLIM) produces spatial maps of the excited state dynamics of fluorophores that can be used to distinguish between different fluorophores, between different microenvironments of the same fluorophore, and between different molecular states of the fluorophore.[1] This enables FLIM to report a wide range of biomolecular processes such as protein-protein interactions read out by Förster resonance energy transfer (FRET) or changes in the conformation of FRET biosensors.[2] A range of different types of FLIM instrumentation is now commercially available that can broadly be categorised according to the type of detectors used. The most common approaches have been laser scanning microscopy combined with time correlated single photon counting (TCSPC) and wide-field microscopy combined with gated or modulated optical intensifiers, although other techniques can also be considered.[3] When deciding which type of FLIM instrument is best suited to a particular scientific question, key considerations are spatial resolution, field of view, and acquisition speed. TCSPC is straightforward to implement on standard laser scanning confocal or multiphoton microscopes that inherently provide optical sectioning and can offer high sensitivity and time resolution, depending on the detector employed. It is a shot-noise limited technique and so provides the highest signal/noise ratio per photon emitted by the sample but is limited in imaging speed by the detection electronics, which impose a maximum photon detection rate constrained by the system dead time, and the onset of photobleaching and/or photo-toxicity as the excitation power is increased. Higher detection rates can be realised in scanning microscopes by sharing the detected photoelectrons between multiple TCSPC channels[4] or by parallelising the process through simultaneously scanning multiple excitation beams and detecting in multiple TCSPC channels.[5,6] Alternatively, parallelised TCSPC can be applied to wide-field detection using, e.g., arrays of single-photon avalanche diode (SPAD) detectors and TCSPC detection.[7]

Wide-field FLIM detection, e.g., using gated or modulated image intensifiers, can be considered as highly parallel FLIM pixel acquisition and permits faster image acquisition for a given excitation intensity. However, these approaches are less photon efficient where they entail sampling the fluorescence decay profiles and typically add excess noise so that they are not shot noise-limited. Nevertheless, the large number of pixels ($>256 \times 256$) acquired in parallel confers significant improvements in acquisition speed and these techniques therefore offer a higher signal to noise ratio per unit acquisition time. Optical sectioning can be realised with wide-field FLIM using spinning disc tandem confocal scanners,[8] using structured illumination,[9] or using light sheet microscopy.[10] Wide-field FLIM can be implemented in the time domain using gated optical image intensifiers[11,12] (GOI) or in the frequency domain using a modulated intensifier[13] or using modulated CMOS detectors.[14,15] While time domain and frequency domain approaches can, in principle, offer similar performance provided the modulation frequencies are high enough, time-gated detection offers the ability to vary the width, spacing, and readout camera integration time of the time gates throughout a decay profile in order to more efficiently sample the fluorescence[16] and is inherently compatible with convenient (mode-locked) pulsed excitation lasers, which can present challenges associated with aliasing in frequency domain systems.[17,18] The use of image intensifiers impacts the achievable spatial resolution owing to the pixellation of their microchannel plates (MCPs) that is typically less fine than the pixellation of the CCD readout cameras, although small pore MCP intensifiers have been reported.[19,20] The spatial resolution of intensifiers is also limited by the lateral spread

[a)]H. Sparks and F. Görlitz contributed equally to this work.

of electrons on their path between the photocathode and the MCP and between the MCP and the phosphor. The reduction in spatial resolution can be minimised by using a high accelerating potential between the photocathode and the MCP to minimise the transit time. However, in wide-field frequency domain FLIM where the photocathode-MCP voltage of an image intensifier is sinusoidally modulated, this photocathode-MCP voltage is lower than its maximum value for much of the modulation period.[21] Modulated CMOS cameras can enable frequency domain FLIM with a higher spatial resolution than intensifier-based systems and are now available with modulation frequencies up to 50 MHz.[22,23]

With an increasing number of technologies being developed for FLIM, it is important to understand the state-of-the-art for different approaches. This paper focusses on wide-field time-gated FLIM, describing new developments in the GOI technology that improve performance. Figure 1 presents a schematic of a typical GOI, showing the photocathode at which the fluorescence photons are incident, the microchannel plate (MCP) that amplifies the photoelectron signal emitted by the photocathode, and the phosphor that converts the electron cascades emerging from each channel of the MCP. The intensifier unit from photocathode to phosphor is enclosed in a vacuum tube.

II. STRATEGIES TO IMPROVE TIME-GATED FLIM

For all FLIM instruments, the temporal resolution depends on the impulse response function (IRF) of the instrument (related to its measurement bandwidth) and the signal to noise ratio. FLIM data are typically analysed by convolving the decay model with the IRF and fitting this to the experimental data. The ability to measure fast fluorescence dynamics then depends on the rising and falling edges of the IRF rather than its total width. For TCSPC, the most commonly used detectors are photomultiplier tubes (PMTs) presenting an IRF with a FWHM of ~150 ps. MCP-PMTs provide FWHM as short as ~30 ps and lower cost hybrid detectors are now available with a FWHM below 40 ps. For TCSPC, the signal to noise ratio scales with $\sqrt{N}$, where N is the number of detected photons and the standard deviation of lifetime measurements of a fluorophore exhibiting a monoexponential decay has formally been shown to vary as $\sqrt{N}$.[24] For time-gated FLIM, the IRF of the GOI can be shorter than 100 ps[25] and the signal to noise ratio also scales with $\sqrt{N}$ but is reduced by an excess noise factor, E. For measurements of a fluorophore exhibiting a monoexponential decay, the standard deviation on the measured lifetime has been shown to scale with $E\sqrt{N}$, where E decreases as the gain voltage across the microchannel plate increases.[26] E is typically less than 1.5 for the high gain voltages (>700 V) typically used for FLIM to ensure that the signal detected from the GOI phosphor for a single detected photon is higher than the noise of the readout CCD camera. Finally, for both TCSPC and time-gated FLIM, decays are measured by averaging over multiple laser excitation pulses, and it is therefore also important that the jitter of the recorded photon arrival times or gate edges, respectively, is as small as possible as it contributes to the overall temporal resolution.

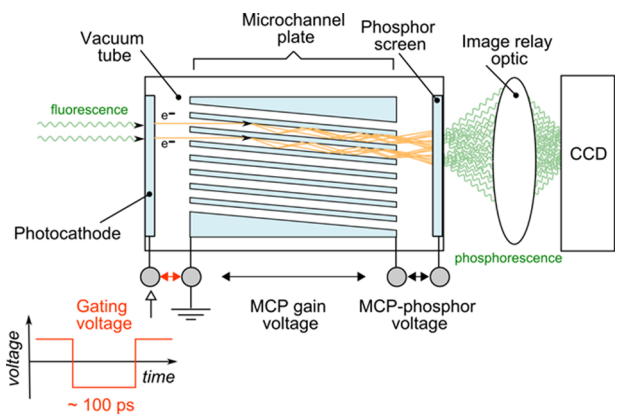

FIG. 1. Schematic of gated optical image intensifier (GOI) used for time-gated FLIM.

To maximise the precision of lifetime determination with time-gated FLIM, it is therefore desirable to use instruments with fast IRF rising and falling edges (i.e., fast detection bandwidth) but with long gate widths for efficient use of fluorescence signal.[16] A commonly used GOI sold for use with MHz repetition rate excitation lasers is made by Kentech Instruments Ltd. (model: HRI, also utilised in the PicoStar from LaVision GmbH) who also makes associated time delay units (models HDG and HDG800). These GOIs are designed to provide quasi-rectangular gate widths ranging from 200 ps to 1 ns in normal operation. However, since most commonly used fluorophores have fluorescence decays with lifetimes significantly longer than 1 ns, it is desirable to develop new GOIs with longer gate widths. In Section II A we present the evaluation of a new prototype GOI able to provide gate widths up to 10 s of ns. We note that it is possible to configure the (Kentech Instruments Ltd., model HRI) instrument to provide gate widths up to ~2.3 ns but this is a non-standard setting and may require optimisation of the cathode bias voltage settings.

A further issue for time-gated FLIM is spatial resolution that is limited primarily by the photoelectrons spreading out on their path from the photocathode to the MCP of the GOI. For the "standard" HRI from Kentech Instruments Ltd., this spatial resolution is typically <25 lp/mm measured at 3% contrast. With a GOI aperture of 18 mm, the time-gated images are usually read out with a CCD camera binned to 256 × 256 pixels. As discussed in Section II B, we have shown that the use of a magnetic field along the axis of the GOI can reduce this spreading out of the photoelectrons by restricting radial drift during their passage to the MCP.

A. Increasing signal using longer time gates

To increase the signal/noise ratio for time-gated FLIM, a new prototype "HRI-HL" was developed with the capability to provide both "standard" gate operation with gate widths ranging from 200 ps to 1 ns and a second "long gate" mode for longer gate widths ranging from 1 ns to 10 s of ns. An important feature of the longer gates is that they retain the same (~100 ps) steep rising and falling edges of the standard gate widths. Figure 2 shows the IRF profiles of a standard HRI and this new HRI-HL model in the standard gate width and in a longer gate width mode.

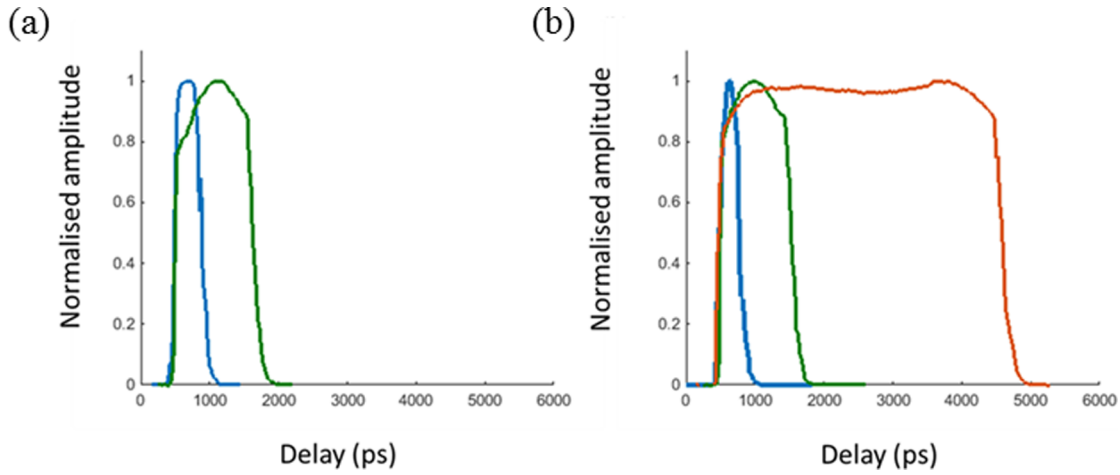

FIG. 2. IRF profiles recorded with ultrafast supercontinuum excitation source and (a) standard HRI with 200 ps and 1000 ps gate widths; (b) HRI-HL in standard mode with 200 ps and 1000 ps gate widths in a long gate mode with a 4000 ps gate width.

To demonstrate that using longer gate widths results in superior performance in terms of lifetime determination, we measured reference samples of Rhodamine B and Rhodamine 6G solutions for a range of gate widths using the automated wide-field multiwell plate FLIM microscope[27–29] described in Sec. IV and using our open source software, FLIMfit.[30] We chose to use these dyes because they present monoexponential decay profiles with respective lifetimes of approximately 1.5 ns and 4 ns that are within the range of lifetimes of fluorescent proteins that are widely used in the FLIM and FRET experiments. To compare the relative performance for different gate width settings, the excitation power at the sample plane and the MCP gain voltage were fixed for all measurements to 180 μW and 750 V, respectively. The acquisition gating strategy was also fixed with each of seven time-gated images acquired with a total of 200 ms integration time. For each gate width setting, the CCD exposure time was adjusted to almost fill the CCD wells at the peak of the fluorescence signal. For the 200 ps gate width, a 200 ms exposure was required to saturate the CCD bit depth when imaging the Rhodamine 6G solution while for longer gate widths, the CCD was saturated more quickly, since more photons were detected, and so a number of CCD frames with shorter exposure times were accumulated to reach the same total exposure time of 200 ms.

Figure 3 shows the resulting lifetime histograms and clearly indicates how the longer gate widths improve the precision of lifetime determination for a given light dose and total acquisition time. This is quantified in Table I, which gives the mean lifetime (τ), standard deviation ($\Delta\tau$), and precision ($\tau/\Delta\tau$), for the measurements of each dye and gate setting. The benefit conferred by longer gate widths is more pronounced for the longer lifetime dye, Rhodamine 6G, for which a significant fraction of the fluorescence signal would arrive outside a 1 ns time gate.

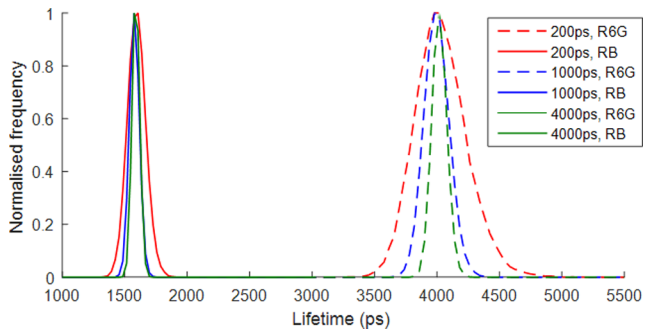

FIG. 3. Lifetime histograms obtained with the HRI-HL for pure wells of RB and R6G for 200, 1000, and 4000 ps gate widths and for an MCP gain voltage of 750 V.

B. Increasing spatial resolution

The relay of the fluorescence image to the readout camera of the GOI begins with "proximity focussing," where a gating voltage accelerates photoelectrons generated at the photocathode to the front face of the MCP. At the MCP, photoelectrons enter discrete channels. Since the photoelectrons will have a velocity distribution that also includes transverse components, during their transit to the MCP, they will spread out causing the spatial resolution achieved to be degraded. Longer gate widths will lead to a higher spatial resolution since the average accelerating voltage during the gate "on" time will be larger as the opening and closing phases of the gate occupy a smaller fraction of the total gate width. Thus increasing the gate width improves both the signal to noise ratio and the spatial resolution for time-gated imaging using a GOI. In the limit, operating a GOI in DC mode (i.e., accelerating voltage always on) will produce the highest spatial resolution. This trend is illustrated in Figure 4, which shows spatial contrast transfer functions (see Sec. IV) and bar charts of the spatial frequencies corresponding to 50% and 3% contrast for a standard HRI. The trend of increasing spatial resolution with increasing gate width is clear.

The loss of spatial resolution due to transverse drift of the photoelectrons in a HRI can be countered by adding a quasi-solenoidal magnetic field aligned along the optical axis of the HRI to guide photoelectrons along helical trajectories about their principal direction.[31] The magnetic field can be chosen so that the photoelectrons on average make one complete turn of the helical trajectory between the photocathode and the MCP. Figure 5 shows the effect of introducing such a magnetic field around and through the GOI tube as realised in a new type of GOI denoted "HRI-S." For comparison, the measurements of

TABLE I. Quantification of fluorescence lifetime measurements of Rhodamine B (RB) and Rhodamine 6G (R6G) using the HRI-HL gated optical image intensifier operated with an MCP gain voltage of 750 V (all quantities in units of picoseconds).

Gate width	RB lifetime	Standard deviation	Precision	R6G lifetime	Standard deviation	Precision
200	1595	74	21.6	3998	224	17.84
1000	1579	39	40.5	3968	118	33.6
4000	1581	32	49.4	3989	72	55.4

spatial contrast transfer functions and spatial frequency values at 50% and 3% contrast are shown for the same GOI with and without the magnetic field. For the sub-nanosecond gate width, where the average gating voltage is much less than its peak value, there is a very significant improvement in spatial resolution when the magnetic field is present. In fact, the magnetic field enhances the spatial resolution for the sub-nanosecond gate width beyond that realised with the 1 ns gate width. This is because the helical trajectory of the photoelectrons that is imposed by the magnetic field is optimal for a gating voltage that is slightly lower than the peak voltage during the gate "on" time.

It is useful to combine both the magnetic field enhancements of the spatial resolution with the increased signal to noise ratio conferred by the longer time gates. To this end, a new GOI, designated "HRI-HL-S," has been developed that offers improved spatial resolution for all gate widths and provides improved light collection efficiency with time gates up to ~10 ns. Figure 6 compares the spatial resolution of a HRI-HL with a HRI-HL-S showing improved spatial resolution across a range of gate widths.

Comparing the 500 ps and 1 ns gate widths between Figures 5 and 6, it is apparent that the HRI-HL has a better spatial resolution than the standard HRI for a given gate width. For the two HRIs with the magnetic field applied, namely, the HRI-S and the HRI-HL-S, the HRI-HL-S has a better spatial resolution for the 3% contrast values. This is attributed to differences between the specific HRI units. As is typical with image converter tubes, there is some spread in the photocathode characteristics together with some variation in the PC to MCP gap. Moreover, the HRI-HL gate drive circuitry is modified with respect to the HRI and the slightly higher spatial resolution of the HRI-HL is attributed to these factors.

To illustrate how the spatial resolution improvement of the new HRI impacts image quality, we implemented FLIM using the standard HRI and the HRI-HL-S with a Nipkow disc scanner unit coupled to an inverted epifluorescence microscope with a 40 × air (NA = 0.6) objective lens. This configuration is widely used where rapid optically sectioned FLIM is required and forms the basis of our automated multiwell plate FLIM microscope.[28] Figure 7 shows optically sectioned images of a dye stained section of Convallaria acquired with the same instrument settings for both HRIs (1 ns gate width; 180 μW excitation power at the sample plane; MCP gain voltage of 750 V; time-gates at delays of 6250 ps, 7000 ps (peak intensity), 7525 ps, 8200 ps, 9075 ps, 10 275 ps, 12 375 ps, and 16 500 ps). Five camera integrations were accumulated at each gate delay for each HRI with the camera exposure times set to ensure similar filling of the cameras bit depth at each gate delay, with the average pixel value at the peak of the fluorescence intensity being more than 50% of the camera's bit depth. The total acquisition times were 20 and 24 s for the standard and HRI-HL-S, respectively. In Figure 7(a), a clear improvement in image sharpness can be seen for the HRI-HL-S FLIM image, which is highlighted by the three expanded views. To further illustrate the improved spatial resolution, Figure 7(c) shows intensity line profiles taken from the integrated intensity images shown in Figure 7(b).

III. DEMONSTRATION OF THE PERFORMANCE OF NEW FLIM INSTRUMENTATION

We are particularly interested in rapid FLIM, e.g., for readouts of FRET and of changes in cellular metabolism in live cells and in automated multiwell plate assays. We believe that multiwell plate FLIM assays of standardised samples

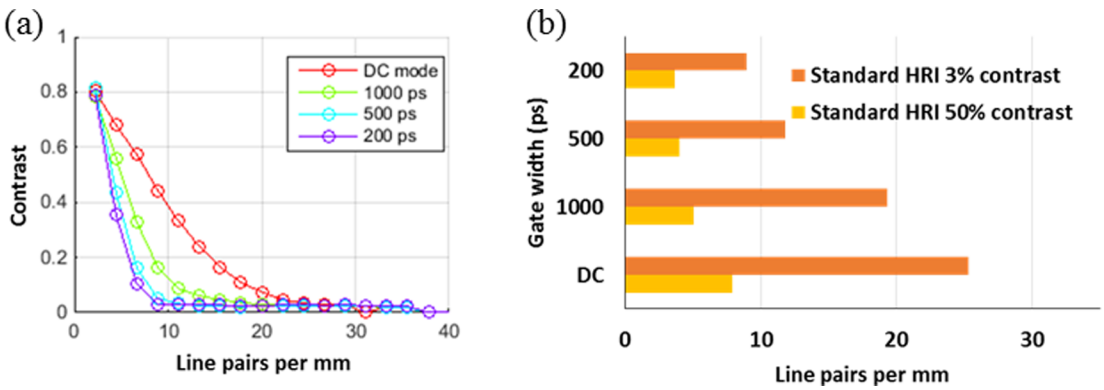

FIG. 4. Spatial resolution for the standard HRI operating with 750 V gain voltage for increasing gate widths. Plot (a) shows the contrast plots for each gate width and the bar chart (b) shows frequencies at which 3% and 50% contrast values are reached for data plotted in (a).

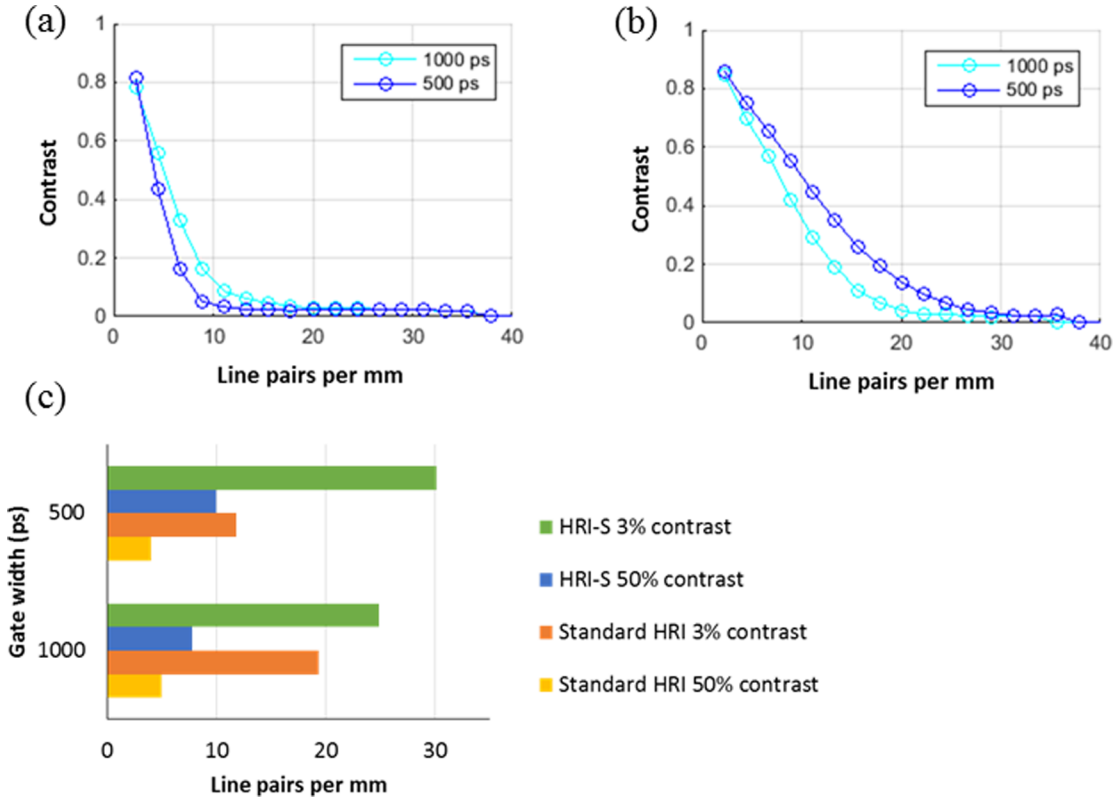

FIG. 5. Comparison of spatial resolution between a standard HRI unit (a) and the same unit with a magnetic field applied—labelled HRI-S (b). Bar chart (c) shows frequencies at which 3% and 50% contrast values were achieved for data plotted in (a) and (b).

can provide a way to compare different approaches to FLIM. Below, we show the comparison between wide-field time-gated FLIM with the established GOI model HRI and the new HRI-HL-S using dye mixtures and cells transfected with mixtures of FRET constructs. Rather than validating absolute lifetime measurements, which are prone to variations in preparation protocol, contamination, and environment (e.g., temperature), we here quantify the ability of the FLIM system to determine the ratio of fluorophores mixed together. Dye solutions can provide a simple and easily reproducible standard sample but their brightness, photostability, and homogeneity make them rather less challenging than live cells labelled with fluorescent proteins, which feature widely in biological applications of FLIM.

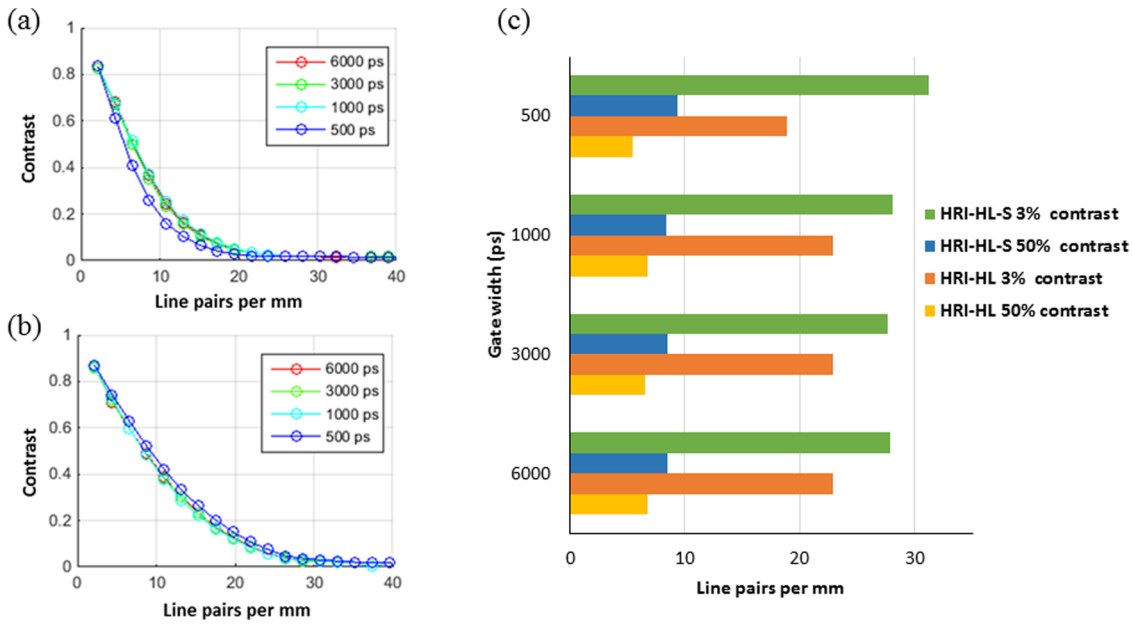

FIG. 6. Comparison of spatial resolution between (a) HRI-HL and (b) new HRI-HL-S for a range of gate widths. Bar chart (c) shows frequencies at which 3% and 50% contrast values were achieved for data plotted in (a) and (b).

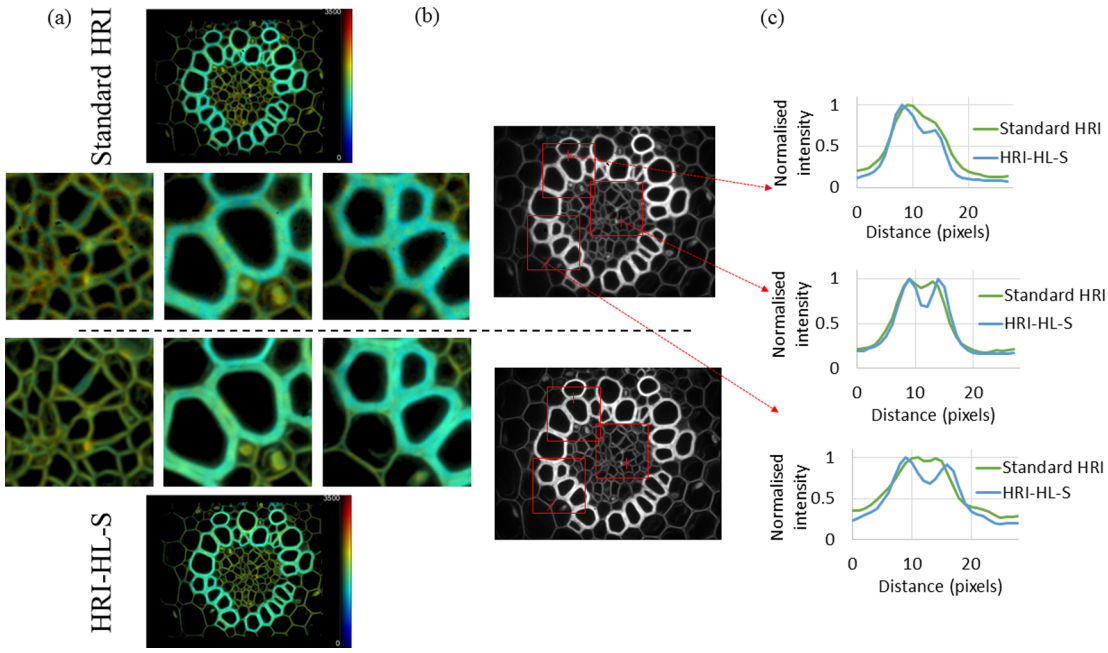

FIG. 7. (a) Intensity merged fluorescence lifetime and (b) time-integrated fluorescence intensity images of the stained Convallaria sample with higher magnification FLIM sub-images from regions indicated in intensity image for standard HRI (upper figures) and new HRI-HL-S (lower figures) together with line profiles (c) indicating improvement in spatial resolution.

A. FLIM of dye mixtures to benchmark performance

Following previous work using multiwell well plate arrays of dye mixtures,[28,32,33] a FLIM-FRET assay was simulated by mixing two dyes that present mono-exponential decay profiles, Rhodamine B (RB) and Rhodamine 6G (R6G), in different ratios to test the ability of the instrument to distinguish the relative contributions of different lifetime components. We used our in-house written software, FLIMfit to unmix the dye fractions by applying global analysis to fit the FLIM data (see Sec. IV). This experiment was undertaken using both the standard HRI and the new HRI-HL-S to compare their performance, including how the use of longer gate widths improves the precision of lifetime determination. To ensure that other factors were equivalent, we set the excitation power at the sample to 180 μW and the total CCD exposure time to 1.6 s across these experiments.

To illustrate the high precision of the lifetime measurements, Figure 8 shows exemplar wide-field time-gated multiwell plate FLIM data automatically acquired using a 20× microscope objective. The total acquisition time for this multiwell plate FLIM data was 15 s per field of view, which included the autofocus, translation stage motion, and CCD image acquisition time (set to 200 ms exposure time at each of the time gate delays used) resulting in a total of 72 min to automatically read 3 FOV in each of 96 wells. Figure 8(b) shows the mean fluorescence lifetime of RB and R6G recovered by global fitting to a double exponential decay model using FLIMfit as discussed in Sec. IV. A comparison of the performance is presented between the standard HRI and the new HRI-HL-S both with 1 ns time gates in Figure 8(c) and between 4 ns and 1 ns time gates using the new HRI-HL-S in Figure 8(d).

To illustrate the precision of determination of the dye fractions, the standard deviation for the measured R6G fractions for each mixture is plotted in Figure 9. For 1 ns gate widths, the new HRI-HL-S presents a lower standard deviation on measured fractions than the standard HRI. Since the time gates are equal, this difference may be attributed to the photocathode of the HRI-HL-S having a higher quantum efficiency. The comparison between the performance of the new HRI-HL-S using 1 ns and 4 ns time gates shows an improvement in precision as expected.

B. FRET constructs to benchmark performance

To demonstrate the performance of the HRI-HL-S GOI for the application to FRET readouts in cells expressing fluorescent protein labels, we used the genetically expressed FRET constructs such as those reported by Koushik *et al.*[34] where cyan fluorescent protein (Cerulean) donor fluorophores are linked by short amino acid sequences to yellow fluorescent protein (Venus) acceptors—or to a non-fluorescent protein (Amber) to provide a negative control. We have adapted these FRET constructs to incorporate mTurquoise fluorescent protein (mTqFP) rather than Cerulean since this has been reported to present a more monoexponential decay profile,[33] which simplifies the fitting model for FLIM. To evaluate the performance of our time-gated FLIM systems for FRET, we transiently transfected a 96 well plate array of HEK293T cells in which each column contained repeated wells expressing a mixture of an mTqFP-Venus FRET construct with a 17 amino acid long linker and the non-FRETing mTqFP-Amber construct with a 5 amino acid long linker. The plasmids were mixed by weight with the ratios indicated in Figure 10 such that the ratios across the columns nominally varied in 10% steps. We note that we have previously observed a linear relationship between weight of plasmid and the intensity of the expressed fluorescent protein.[35]

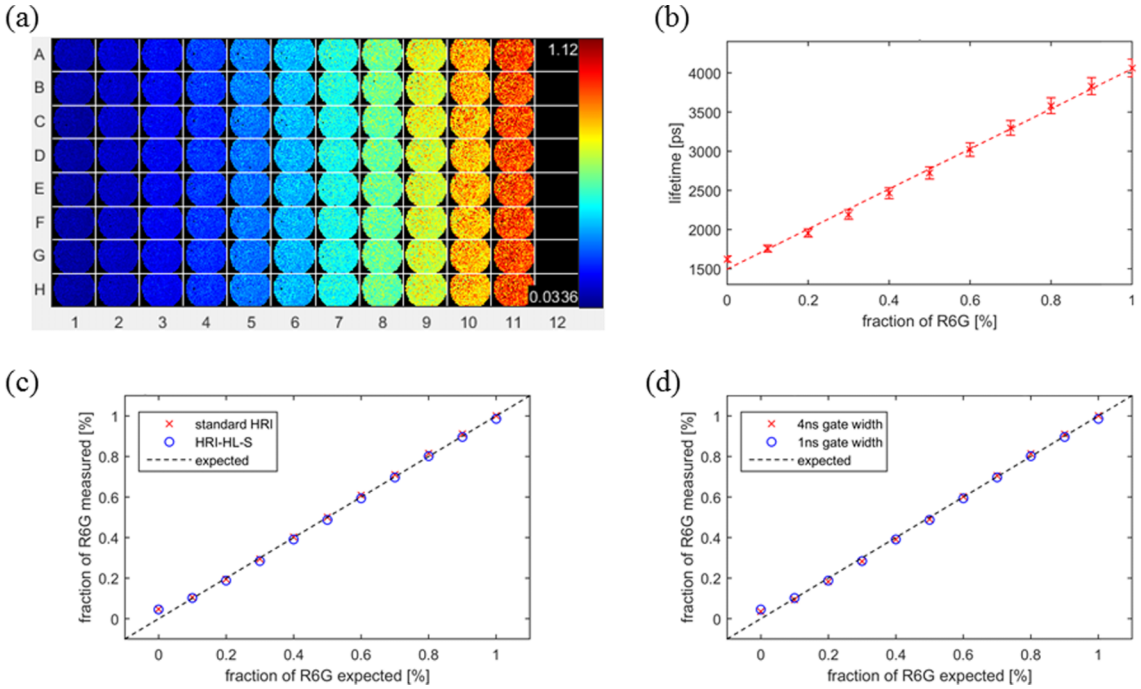

FIG. 8. Wide-field time-gated FLIM data: (a) montage showing the mean fluorescence lifetime image of one field of view from each well; (b) plot of mean lifetime averaged over all FOV for each dye mixture as a function of mixing ratio acquired with new HRI-HL-S using 4 ns time gates; ((c) and (d)) R6G/RB dye ratio obtained by global fitting for FLIM data (c) acquired with 1 ns gates for the standard HRI and new HRI-HL-S and (d) acquired with new HRI-HL-S using 1 ns and 4 ns time gates.

The wide-field time-gated multiwell plate FLIM data presented in Figure 10 were automatically acquired using a 20× microscope objective with the incident intensity at the sample again set to 180 μW. The total exposure time for these FLIM data was fixed to 200 ms per field of view. Figure 10 shows the results of applying global fitting to the donor lifetime measurements of this 96 well plate of FRET constructs using a double exponential decay model to describe the decay from mTqFP-Venus and single exponential decay to describe the decay of mTqFP-Amber in *FLIMfit*, see Sec. IV for more details. The analysis returns a measure of the relative contributions of the FRETing and non FRETing mTqFP donor fluorophores. From columns 1 to 11, the concentration of the mTqFP-Venus construct increases from 0% in column 1 to 100% in column 11 while the non-FRETing mTqFP-Amber construct decreases from 100% to 0%. Figure 10(c) shows the measured mean fraction of mTqFP-Venus plotted against the expected value calculated from the respective weights of the plasmids used for the transfection. The expected trend of low FRET in column 1 to high FRET population fraction in column 11 is seen. Figure 10(d) shows the standard deviation measured per pixel for the relative fraction of mTqFP-Venus.

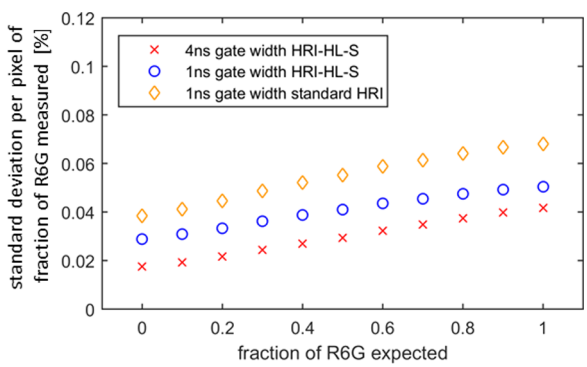

FIG. 9. Wide-field time-gated FLIM data showing the standard deviation in measured R6G fraction calculated per pixel and plotted as a function of dye ratio for standard HRI and new HRI-HL-S using 1 ns time gates and 4 ns time gates.

To further illustrate the potential impact of this improved capability for cell biology experiments, we show in Figure 11 how the weighted mean and standard deviation of the donor fluorescence lifetime of the mTqFP-VFP FRET construct expressed in HEK cells vary as a function of excitation intensity (and therefore as a function of the number of detected photons) as the excitation beam is attenuated using neutral density (ND) filters. For this experiment, a separate set of cells—arrayed in 6 wells across a row of a multiwell plate—was imaged for each setting of excitation power in order to eliminate any artefacts that could arise from repeatedly imaging the same cells. Each row was imaged twice, once with a 1 ns gate width and once with a 4 ns gate width. For each gate width, 6 views were imaged per well so a total of 36 views per ND filter setting per gate width were collected. Figure 11 illustrates that the precision of lifetime determination decreases with decreasing excitation power and that the FLIM acquisitions with 4 ns gate widths provide smaller standard deviations of the weighted mean donor lifetime of the mTqFP-VFP FRET construct. We note that for ND = 2, the signal was so low that we could not obtain any meaningful lifetime values from the measurement with the 1 ns gate width.

To illustrate the spatial resolution improvement provided by the HRI-HL-S compared to the standard HRI when imaging cell samples, the optically sectioning FLIM microscope

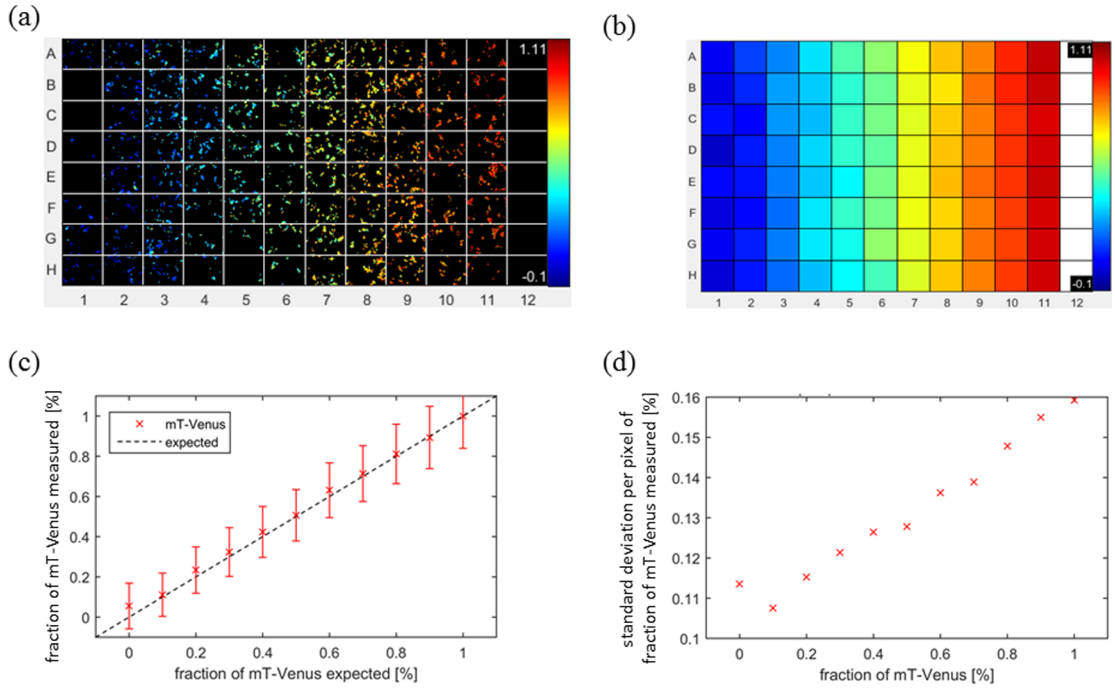

FIG. 10. Wide-field time-gated FLIM data: (a) FRETing donor fraction images for one exemplar field of view for each condition; (b) mean FRETing population fraction indicated by global fitting of FLIM data; (c) plot of the mean measured FRETing donor population fraction per condition against the predicted mTqFP-Venus fraction based on plasmid weight ratio of the two constructs, error bars show the pixel-wise standard deviation in donor population fraction; (d) corresponding pixel-wise standard deviation (STD) for the experimentally measured value of FRETing population fraction as a function of predicted mTqFP-Venus fraction.

described in Section II B was used to image HEK293T cells expressing an mTqFP-Venus construct. Figure 12 shows optically sectioned "donor" images for which a clear improvement in spatial resolution is evident, as can be seen in the sharpness of the cell boundaries and improved visibility of filopodia-like structures.

IV. MATERIALS AND METHODS

A. Spatial resolution measurements

The resolution of an incoherent optical system can be described by the efficiency with which it transfers spatial frequencies in intensity. The equation for defining the contrast transfer function, C, as a function of spatial frequency k is

$$C(k) = \frac{I_{max} - I_{min}}{I_{max} + I_{min}}. \quad (1)$$

The experimental setup for measuring the spatial resolution of the FLIM instrumentation is shown in Figure 13. The radial test chart (Edmund Optics, #58-833) shown in Figure 13(a) was uniformly illuminated using an LED and a rotating diffuser and circular line profiles such as those shown in Figure 13(b) were used to determine contrast values from Equation (1). As shown in Figure 13(c), the test chart was imaged onto the GOI photocathode via lens L3 (1" diameter

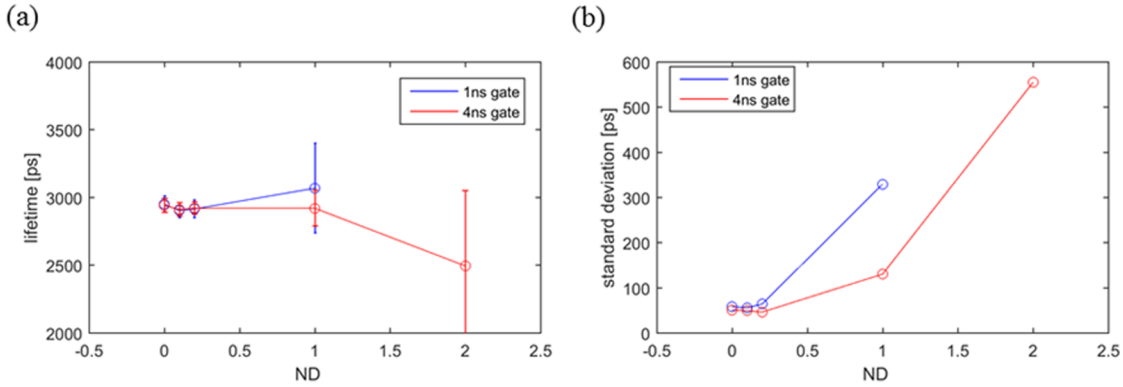

FIG. 11. Variation of (a) weighted mean and (b) standard deviation of donor fluorescence lifetime as a function of CCD camera integration for HEK cells expressing an mTqFP-YFP FRET construct with the fluorescence decay profiles fitted to a biexponential decay model. The fluorescence decay data were fitted using a global double exponential decay model with the lifetime components determined across each field of view and the pre-exponential factors determined pixel-wise. Values were calculated field of view-wise with 6 views per well and 6 wells per ND filter setting. Error bars shown in (a) are the standard deviation over the values returned for each field of view and the same values are plotted separately in (b).

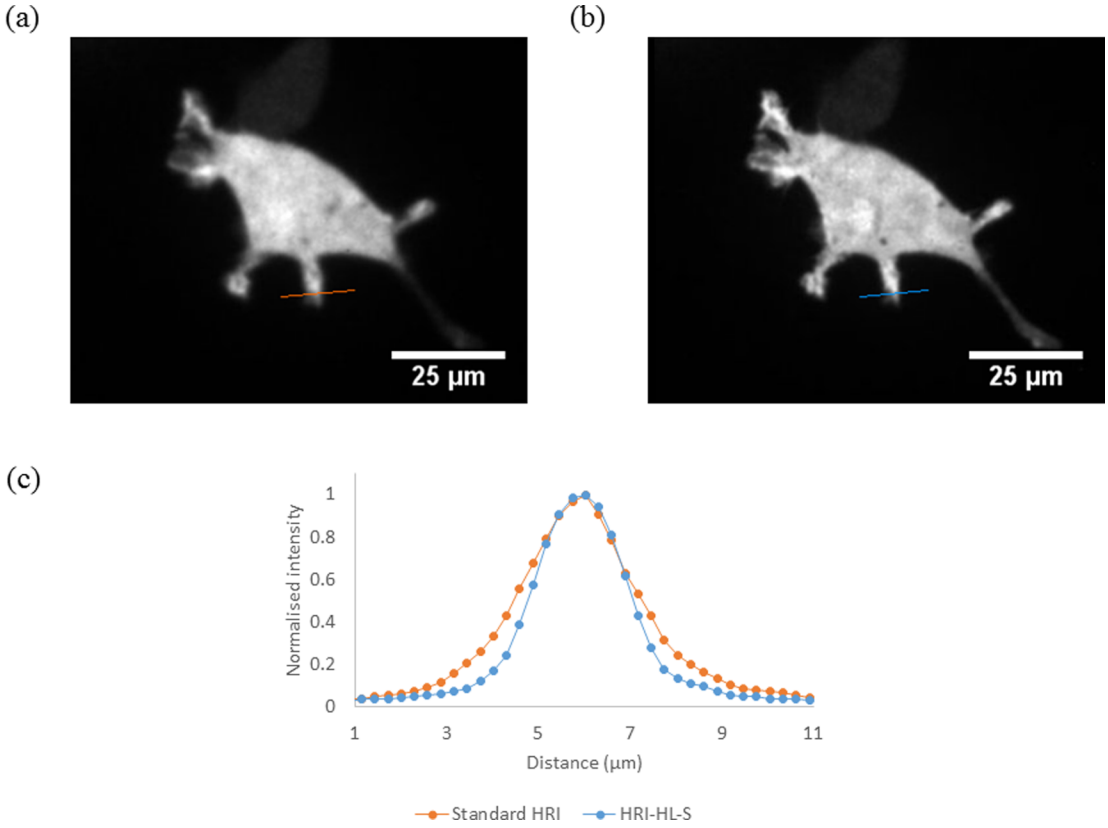

FIG. 12. Optically sectioned time-gated intensity images of HEK293T cells expressing an mTqFP-Amber FRET construct imaged using a standard HRI, (a) and the new HRI-HL-S, (b) acquired with 1000 ps gate widths with indicated line scans, (c) illustrating improved spatial resolution of HRI-HL-S.

visible achromat, 60 mm focal length (Thorlabs, AC254-060-A-ML)), with a magnification of 2, which was fixed for all experiments. In order to minimise the effect of Poisson noise on measured contrast values, CCD images were averaged over 100 frames.

B. Experimental setup for the measurement of FLIM performance

Figure 14 shows the experimental configuration used here for wide-field time-gated FLIM. Please see the work of Kelly *et al.*[29] for a full description of the system. For the dye measurements, the ultrashort pulse radiation from a 40 MHz fibre laser-pumped supercontinuum laser (Fianium UK Ltd., SC400-4) was spectrally filtered to provide excitation radiation that was delivered via a single mode optical fibre (SMF) to an inverted microscope frame (Olympus, model: IX81) through a dual lamp housing (DLH) attachment. A single mode optical fibre is used to deliver the excitation light to the microscope frame rather than a multimode fibre as temperature variations or mechanical perturbations or vibrations of the fibre can introduce slow drifts in the optical path length of the multimode fibre and hence change the absolute timing between the arrival time of the excitation pulse at the sample and the opening of the GOI. Such slow variations introduce systematic errors in the fitted fluorescence lifetime parameters, particularly for extended acquisition such as time courses or multiwell plate experiments.

For automated multiwell plate imaging, 96 well plates were mounted on a motorised microscope stage. Before entering the microscope, the excitation radiation passed through a rotating diffuser (RD) and wire grid polariser (P1) to ensure spatially homogenous and plane polarised excitation. A photodiode (PD) positioned at the diffuser was used to monitor the laser power stability after the delivery fibre.

For FLIM of the dye samples, a 525/50 nm band pass filter was used to select the excitation radiation from the supercontinuum and an RFP filter cube (FC) set (545/50 nm (Ex), 605 nm dichroic, 660/70 nm (Em)) was used. At the exit port of the microscope before the GOI photocathode, a second wire grid polariser was placed between a pair of 40 mm focal length achromatic lenses (Thorlabs, AC254-040-A-ML) in a 4-f configuration. The polarisers were set for "magic angle" detection[1] to avoid fluorescence anisotropy effects from the freely rotating dye molecules in solution.

For FLIM of the cells, expressing mTqFP-based FRET constructs a 434/17 nm band pass filter to select the excitation radiation from the supercontinuum source and a CFP filter cube (438/24 (Ex) 458 dichroic, 483/32 nm (Em)) were used.

The image was relayed from the GOI phosphor by a pair of camera lenses with 50 mm/35 mm focal lengths (Nikon, AF NIKKOR 50 mm, AF NIKKOR 35 mm) onto a cooled scientific camera (ORCA-ER, Japan, Hamamatsu), which was operated in 4×4 hardware binning mode providing 336 $\times$ 256 pixels. To synchronise the GOI with the pulsed excitation laser, the amplified signal from a photodiode inside the laser was used to trigger a slow delay update (Kentech, precision programmable 50 Ω delay line) and fast delay update (Kentech, HDG800) generator. An MCP voltage of 750 V was used for all the measurements presented in this paper.

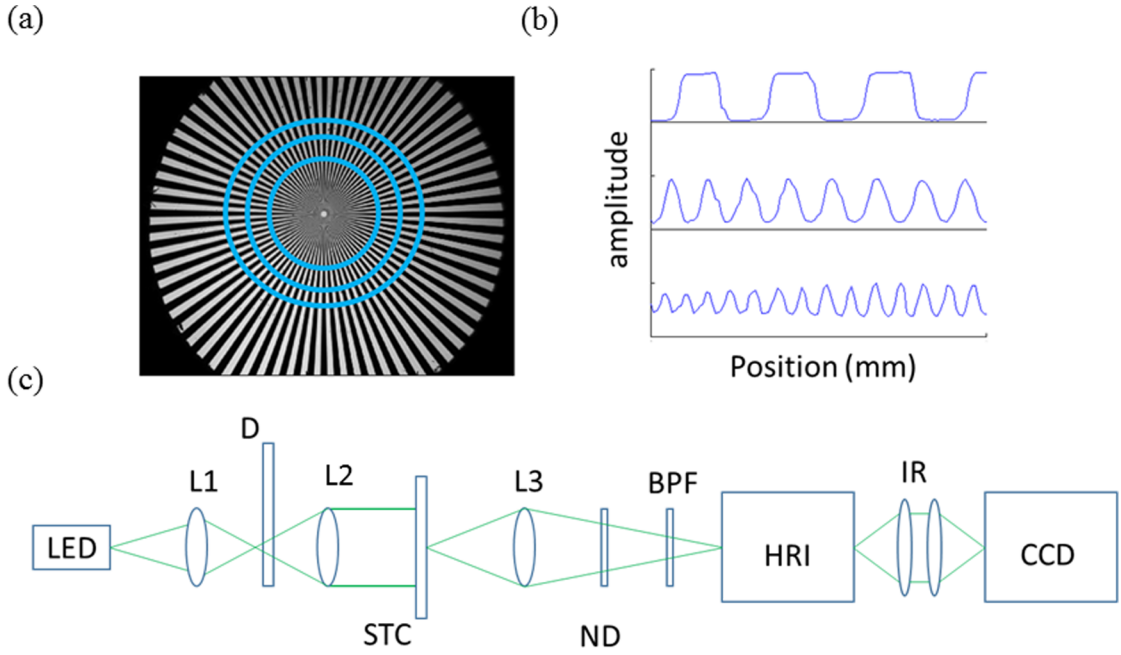

FIG. 13. (a) Radial test chart used to measure spatial resolution; (b) modulation pattern of test chart at different radial distances from centre as indicated by blue circles in (a); (c) optical setup for imaging test chart onto GOI photocathode for spatial resolution measurements. LED, light emitting diode; L1-3 lenses; D, diffuser; STC, star test chart; ND, neutral density filter; BPF, band pass filter; HRI high rate imager; IR, image relay; CCD, charge coupled device.

For the lifetime measurements shown in Section II, Table I, and Figure 3, the fluorescence decay was sampled with seven time gates at delays of 1800 ps, 2800 ps, 3300 ps, 2800 ps (peak intensity), 7600 ps, 10 100 ps, and 11 600 ps. For the subsequent multiwell FLIM of dye mixtures and transfected cells, the decay was sampled using eight time gates at delays of 6250 ps, 7000 ps (peak intensity), 7525 ps, 8200 ps, 9075 ps, 10 275 ps, 12 375 ps, and 16 500 ps.

For optically sectioned FLIM, a spinning Nipkow disc scanner was incorporated before the GOI (Yokogawa, model CSU-X) and a triple band (409-458 nm/520-535 nm/650-672 nm) dichroic and 482/35 nm band pass emission filter were used.

C. Selecting gate delays for time-gated FLIM

To the best of our knowledge, the deterministic optimisation of gating strategies for arbitrary samples to be fitted to complex decay profiles has yet to be reported. In general, it is desirable to minimise the data acquisition time and therefore the number of time gates. However, we note that, if we are fitting two decay components and a background to an experimental decay data set, a minimum of 4 time gates are required to determine the two exponential decays and a further time gate is required to measure the background. We acquire an additional time gate before the excitation pulse as this is helpful in checking that the t0 shift of the decay model being fitted is

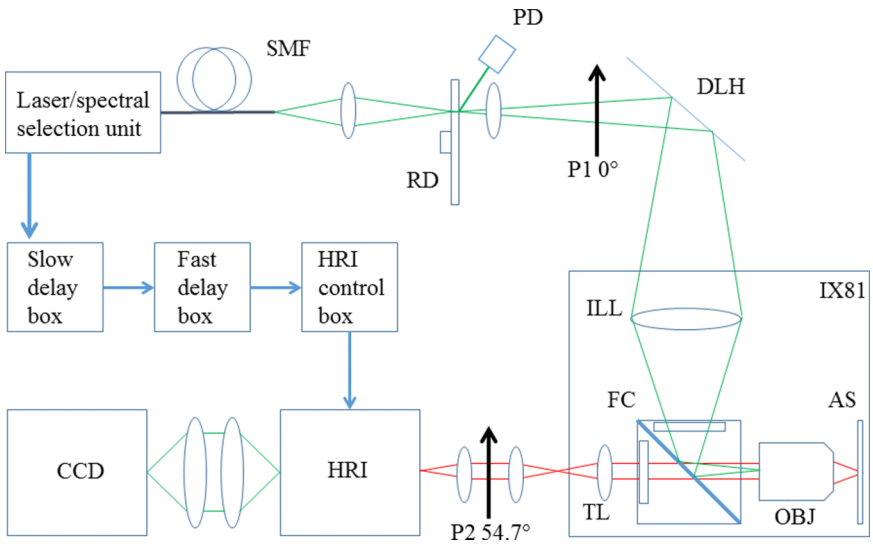

FIG. 14. Experimental setup for wide-field time-gated FLIM. SMF, single mode fibre; RD, rotating diffuser; PD, photodiode; P1-2, linear polarisers; ILL, illumination condenser; FC, filter cube; OBJ, objective; AS, automated sample stage; TL, tube lens; HRI, High Rate Imager; CCD, charge coupled device.

correct. We also choose to acquire a further time gate so that the decay fitting problem is over determined, which reduces the sensitivity of the goodness of fit to the specific lifetime values encountered. We further note that we sample the change in the intensity of the fluorescence decay exponentially in time such that the intensity values are approximately equally spaced.

D. Accounting for spatial variations in the IRF

GOIs can exhibit an "irising" phenomenon that is caused by the time taken for the gating voltage applied between the photocathode and the MCP to propagate from the perimeter of the photocathode to its centre, thereby causing a variation in gate opening time of 10 s of picoseconds across the FOV. (A similar effect also arises when excitation light is delivered by a multimode fibre, e.g., to produce a wide illumination.[36]) As long as these spatial variations can be measured, e.g., by measuring the IRF for every pixel of the image, they can be accounted for in the fitting procedure. For the wide-field FLIM data presented in this paper, we acquired a spatially varying IRF using excitation light reflected from a mirror in the focal plane of the objective. To record scattered excitation light without damaging the detector, a filter cube with a neutral density filter in the emission path and a glass microscope slide as the beam splitter was used to attenuate the detected signal. The resulting spatially varying IRF dataset was then opened in *FLIMfit* and a small region in the centre of the field of view was selected to determine the shape of the IRF. *FLIMfit*[30] then cross-correlates this IRF with every pixel in the spatially varying IRF dataset to produce a map of the variation in gate opening time across the FOV that is then saved and used when analysing FLIM data.

E. Preparation of dye mixture multiwell plate sample

Stock solutions of RB and R6G were made by dissolving pure dye powder in 1 ml spectroscopic grade methanol and then subsequent dilution with 49 ml MilliQ purified water (Millipore, USA) to obtain final stock concentrations of 10 μM for each dye. These solutions were then mixed to prepare the desired ratios in 10 ml of solution and 200 μl per well was pipetted into a plastic bottomed 96 well plate according to the map shown in Table II, i.e., with 8 repeats per mixture in each column such that 88 wells were filled. Purified MilliQ water was pipetted along rows A and H to facilitate measurements of instrument background.

F. Calculation of dye ratios from FLIM data

Following the work of Warren *et al.*,[30] the fluorescence decay of a mixture of two monoexponential fluorophores can be represented as

$$I(t) = I_0\left[\beta e^{-t/\tau_1} + (1-\beta)\, e^{-t/\tau_2}\right], \tag{2}$$

where β_1 and $(1-\beta_1)$ are the fitted normalised pre-exponential factors. This is analogous to an ideal FRET measurement with two monoexponential donors such that the two lifetime components represent "FRETing" and non-"FRETing" sub-

TABLE II. 96-well plate map for dye mixtures as a fraction of Rhodamine 6G relative to Rhodamine B.

	1	2	3	4	5	6	7	8	9	10	11	12
A	0	0.1	0.2	0.3	0.4	0.5	0.6	0.7	0.8	0.9	1	X
B	0	0.1	0.2	0.3	0.4	0.5	0.6	0.7	0.8	0.9	1	X
C	0	0.1	0.2	0.3	0.4	0.5	0.6	0.7	0.8	0.9	1	X
D	0	0.1	0.2	0.3	0.4	0.5	0.6	0.7	0.8	0.9	1	X
E	0	0.1	0.2	0.3	0.4	0.5	0.6	0.7	0.8	0.9	1	X
F	0	0.1	0.2	0.3	0.4	0.5	0.6	0.7	0.8	0.9	1	X
G	0	0.1	0.2	0.3	0.4	0.5	0.6	0.7	0.8	0.9	1	X
H	0	0.1	0.2	0.3	0.4	0.5	0.6	0.7	0.8	0.9	1	X

populations and β is the FRETing population fraction. We note that Equation (2) can be modified to include a background term but, for these relatively bright dye samples, no background fluorescence was apparent.

In order to relate the fitted fractions of dyes to those expected from the molar mixing ratios of the prepared solutions, we need to account for the relative brightness of each dye, which depends on their respective spectral properties and quantum yields. This can be done using the following equation:

$$I(t) = A_{\mathrm{R6G}}\beta e^{-t/\tau_{6G}} + A_{RB}(1-\beta)\cdot e^{-t/\tau_{RB}}, \tag{3}$$

where the pre-exponential factors A_{R6G} and A_{RB} can be determined from the measurements of pure solutions of each dye under the same conditions that are fitted to a monoexponential decay model to obtain the brightness per mole given by $C_i = {}^{A_i}/_{M_i}$, where M_i represents the molar concentration.

The relative contributions A_{R6G} and A_{RB} for a mixture of the two dyes can then be calculated using

$$\begin{aligned} A_{RB} &= \frac{C_{RB}M_{RB}}{C_{RB}M_{RB} + C_{\mathrm{R6G}}M_{\mathrm{R6G}}}, \\ A_{\mathrm{R6G}} &= \frac{C_{\mathrm{R6G}}M_{\mathrm{R6G}}}{C_{RB}M_{RB} + C_{\mathrm{R6G}}M_{\mathrm{R6G}}}. \end{aligned} \tag{4}$$

G. Preparation of FRET construct mixture multiwell plate samples

HEK293T cells were transfected using X-tremeGENE 9 DNA protocol. Cells were transfected in a 6 well plate and transferred after 24 h to a 96 well plate. The cells rest there for another 24 h before being imaged in HBSS media. To set up the multiwell plate array with different FRET construct ratios, 11 different vials were prepared with protocol volumes of OptiMEM, X-tremeGENE 9 DNA, and plasmid DNA, with the plasmid DNA for mTqFP-Venus and mTqFP-Amber being mixed in the desired ratios according to weight (measured using a [Thermo Scientific] Nanodrop Lite). We assumed that the plasmid weights were the same for each construct and that they would be expressed by cells with equal efficiency. For the data presented in Figure 11, HEK cells were transfected only with

the plasmid DNA for mTqFP-Venus. For the data presented in Figure 12, HEK cells were transfected with mTqFP-Amber.

H. Calculation of FRETing population ratios from FLIM data

The measured donor fluorescence decay profile of mTqFP-Amber fitted well to a monoexponential decay model but this was not the case for the FRETing construct, mTqFP-Venus, which we therefore fitted to a double exponential decay profile. Thus the resulting fitting model was given by

$$I(t) = I_0\left[\gamma\left(\beta e^{-t/\tau_{11}} + (1-\beta)\, e^{-t/\tau_{12}}\right) + (1-\gamma)\, e^{-t/\tau_2}\right], \quad (5)$$

where β represents the population fraction of the shorter mTqFP-Venus decay component with lifetime τ_{11}, and τ_{12} is the lifetime of the slower mTqFP-Venus decay component. This complex decay profile may be attributed to dark states of the Venus fluorescent protein.[33] The mTqFP-Amber lifetime is represented by τ_2. The different fractions of expressed plasmids are represented by γ.

Global fitting of column 1 only of the plate was performed to determine the values of τ_{11}, τ_{12} and β, resulting in values of 3.1 ns for τ_{11}, 0.7 ns for τ_{12} and 0.64 for β. Global fitting of column 11 only of the plate was performed to determine the value of τ_2 giving a value of 3.8 ns. The data from the whole plate were then fitted globally with the values of I_0 and γ determined for each pixel and all other values fixed to those reported above.

V. CONCLUSIONS

In conclusion, we have demonstrated that the performance of time-gated FLIM instrumentation based on GOI technology can be significantly improved by increasing the width of the time gates and by using a magnetic field to reduce the lateral spread of photoelectrons as they travel between the photocathode and the MCP. We have characterised the performance of a standard (model HRI) and a new GOI (model HRI-HL-S) incorporating new circuitry to permit longer time gates and a magnetic field to improve the spatial resolution. To permit benchmarking of a different FLIM instrumentation, we demonstrated procedures to quantify the ability of the different FLIM systems to discriminate the mixtures of fluorophores presenting different lifetimes including both dye mixtures and cells expressing fluorescent protein-based FRET constructs. The plate based on dye mixtures is easy to prepare but does not exhibit many of the photophysical issues associated with imaging, e.g., fluorescent proteins expressed in cells. These include photobleaching and dependence of the photobleaching rate on peak excitation power. In the future if the sample preparation and image acquisition protocol can be standardised for the plate based on protein-based FRET constructs, e.g., by producing stable cell lines expressing the different ratios of the FRET constructs, we believe that this could be a generally useful approach to compare the performance of different FLIM instruments—noting that it permits comparison of different software tools for FLIM data analysis as well as different hardware components and acquisition protocols.

ACKNOWLEDGMENTS

The authors gratefully acknowledge funding from the UK Engineering and Physical Sciences Research Council (EPSRC EP/I02770X/1 and Imperial College London EPSRC Impact Acceleration Account Pathways to Impact grant) and the UK Biotechnology and Biological Sciences Research Council (BBSRC BB/M006786/1). H.S. and F.G. acknowledge EPSRC funded Ph.D. studentships and S.C.W. acknowledges a Ph.D. studentship from the Institute of Chemical Biology EPSRC funded Doctoral Training Centre.

APPENDIX: DATA AVAILABILITY

Data underlying this article can be accessed on Imperial College London's OMERO server at https://cisbic.bioinformatics.ic.ac.uk/omero/webclient/?show=project-4353 and used under a Creative Commons Attribution licence.

[1]J. R. Lakowicz, *Principles of Fluorescence Spectroscopy* (Springer Science & Business Media, 2007).
[2]T. Gadella, *FRET and FLIM Techniques* (Elsevier, 2009).
[3]E. Gratton, S. Breusegem, J. Sutin, Q. Ruan, and N. Barry, J. Biomed. Opt. **8**, 381 (2003).
[4]J. L. Rinnenthal, C. Börnchen, H. Radbruch, V. Andresen, A. Mossakowski, V. Siffrin, T. Seelemann, H. Spiecker, I. Moll, J. Herz, A. E. Hauser, F. Zipp, M. J. Behne, and R. Niesner, PLoS One **8**, e60100 (2013).
[5]S. Kumar, C. Dunsby, P. A. A. De Beule, D. M. Owen, U. Anand, P. M. P. Lanigan, R. K. P. Benninger, D. M. Davis, M. A. A. Neil, P. Anand, C. Benham, A. Naylor, and P. M. W. French, Opt. Express **15**, 12548 (2007).
[6]S. P. Poland, N. Krstajić, J. Monypenny, S. Coelho, D. Tyndall, R. J. Walker, V. Devauges, J. Richardson, N. Dutton, P. Barber, D. D.-U. Li, K. Suhling, T. Ng, R. K. Henderson, and S. M. Ameer-Beg, Biomed. Opt. Express **6**, 277 (2015).
[7]D.-U. Li, J. Arlt, J. Richardson, R. Walker, A. Buts, D. Stoppa, E. Charbon, and R. Henderson, Opt. Express **18**, 10257 (2010).
[8]D. M. Grant, J. McGinty, E. J. McGhee, T. D. Bunney, D. M. Owen, C. B. Talbot, W. Zhang, S. Kumar, I. Munro, P. M. Lanigan, G. T. Kennedy, C. Dunsby, A. I. Magee, P. Courtney, M. Katan, M. A. A. Neil, and P. M. W. French, Opt. Express **15**, 15656 (2007).
[9]M. J. Cole, J. Siegel, S. E. D. Webb, R. Jones, K. Dowling, P. M. W. French, M. J. Lever, L. O. D. Sucharov, M. A. A. Neil, R. Juškaitis, and T. Wilson, Opt. Lett. **25**, 1361 (2000).
[10]P. Weber, S. Schickinger, M. Wagner, B. Angres, T. Bruns, and H. Schneckenburger, Int. J. Mol. Sci. **16**, 5375 (2015).
[11]X. F. Wang, T. Uchida, D. M. Coleman, and S. Minami, Appl. Spectrosc. **45**, 360 (1991).
[12]K. Dowling, M. J. Dayel, M. J. Lever, P. M. W. French, J. D. Hares, and A. K. L. Dymoke-Bradshaw, Opt. Lett. **23**, 810 (1998).
[13]T. W. J. Gadella, T. M. Jovin, and R. M. Clegg, Biophys. Chem. **48**, 221 (1993).
[14]A. Esposito, T. Oggier, H. C. Gerritsen, F. Lustenberger, and F. S. Wouters, Opt. Express **13**, 9812 (2005).
[15]Q. Zhao, B. Schelen, R. Schouten, R. van den Oever, R. Leenen, H. van Kuijk, I. Peters, F. Polderdijk, J. Bosiers, M. Raspe, K. Jalink, J. G. S. de Jong, B. van Geest, K. Stoop, and I. T. Young, J. Biomed. Opt. **17**, 126020 (2012).
[16]I. Munro, J. McGinty, N. Galletly, J. Requejo-Isidro, P. M. P. Lanigan, D. S. Elson, C. Dunsby, M. A. A. Neil, M. J. Lever, G. W. H. Stamp, and P. M. W. French, J. Biomed. Opt. **10**, 51403 (2005).
[17]E. B. Van Munster and T. W. J. Gadella, J. Microsc. **213**, 29 (2004).
[18]A. D. Elder, C. F. Kaminski, and J. H. Frank, Opt. Express **17**, 23181 (2009).
[19]O. H. W. Siegmund, Nucl. Instrum. Methods Phys. Res., Sect. A **525**, 12 (2004).
[20]A. Martindale, J. S. Lapington, and G. W. Fraser, Nucl. Instrum. Methods Phys. Res., Sect. A **573**, 111 (2007).
[21]H. Chen and E. Gratton, Microsc. Res. Tech. **76**, 282 (2013).

[22]R. Franke and G. A. Holst, Proc. SPIE **9328**, 93281K (2015).
[23]H. Chen, G. Holst, and E. Gratton, Microsc. Res. Tech. **78**, 1075 (2015).
[24]M. Köllner and J. Wolfrum, Chem. Phys. Lett. **200**, 199 (1992).
[25]J. D. Hares, in *31st Annual Technical Symposium*, edited by M. C. Richardson (International Society for Optics and Photonics, 1988), pp. 165–170.
[26]J. McGinty, J. Requejo-Isidro, I. Munro, C. B. Talbot, P. A. Kellett, J. D. Hares, C. Dunsby, M. A. A. Neil, and P. M. W. French, J. Phys. D: Appl. Phys. **42**, 135103 (2009).
[27]C. B. Talbot, J. McGinty, D. M. Grant, E. J. McGhee, D. M. Owen, W. Zhang, T. D. Bunney, I. Munro, B. Isherwood, R. Eagle, A. Hargreaves, C. Dunsby, M. A. A. Neil, and P. M. W. French, J. Biophotonics **1**, 514 (2008).
[28]D. Alibhai, D. J. Kelly, S. Warren, S. Kumar, A. Margineau, R. A. Serwa, E. Thinon, Y. Alexandrov, E. J. Murray, F. Stuhmeier, E. W. Tate, M. A. A. Neil, C. Dunsby, and P. M. W. French, J. Biophotonics **6**, 398 (2013).
[29]D. J. Kelly, S. C. Warren, D. Alibhai, S. Kumar, Y. Alexandrov, I. Munro, A. Margineanu, J. McCormack, N. J. Welsh, R. A. Serwa, E. Thinon, M. Kongsema, J. McGinty, C. Talbot, E. J. Murray, F. Stuhmeier, M. A. A. Neil, E. W. Tate, V. M. M. Braga, E. W.-F. Lam, C. Dunsby, and P. M. W. French, Anal. Methods **7**, 4071 (2015).
[30]S. C. Warren, A. Margineanu, D. Alibhai, D. J. Kelly, C. Talbot, Y. Alexandrov, I. Munro, M. Katan, C. Dunsby, and P. M. W. French, PLoS One **8**, e70687 (2013).
[31]A. Dymoke-Bradshaw, Proc. SPIE **427**, 79 (1984).
[32]A. Esposito, H. C. Gerritsen, and F. S. Wouters, J. Opt. Soc. Am. A **24**, 3261 (2007).
[33]K. A. Walther, B. Papke, M. B. Sinn, K. Michel, and A. Kinkhabwala, Mol. Biosyst. **7**, 322 (2011).
[34]S. V. Koushik, H. Chen, C. Thaler, H. L. Puhl, and S. S. Vogel, Biophys. J. **91**, L99 (2006).
[35]D. Kelly, "An automated fluorescence lifetime imaging plate reader: Application to high content imaging of protein interactions and label free readouts of cellular metabolism," Ph.D. thesis, Imperial College London, 2014.
[36]H. Sparks, S. Warren, J. Guedes, N. Yoshida, T. C. Charn, N. Guerra, T. Tatla, C. Dunsby, and P. French, J. Biophotonics **8**, 168 (2015).